Invariant-embedding R-matrix scheme for reflection high-energy electron diffraction

T. C. Zhao, H. C. Poon,* and S. Y. Tong
Department of Physics and Laboratory for Surface Studies, University of Wisconsin–Milwaukee, Milwaukee, Wisconsin 53201
(Received 8 February 1988)

We present a dynamical theory based on the invariant-embedding R-matrix scheme for calculating reflection high-energy electron-diffraction rocking curves. The method is shown to be accurate and numerically stable. Using Ag(001) and Pt(111) surfaces as examples, we demonstrate the importance of reaching proper numerical convergence in the rocking-curve calculations. The effect of different models for the imaginary potential on rocking curves is presented.

I. INTRODUCTION

In reflection high-energy electron diffraction (RHEED), electrons are elastically backscattered by a solid's surface at grazing incidence. RHEED is the structural probe installed routinely in molecular-beam-epitaxy (MBE) systems. Because of its forward scattering geometry, the technique works well for studying surface structures that are formed during deposition and whose analysis must be performed *in situ* in the deposition chamber. Due to the low Debye-Waller factor in RHEED, it is also the structural technique of choice for studying high-temperature structures. With the current strong interest in the synthesis of new materials by epitaxial molecular growth, there is increasing demand to develop RHEED into a reliable structural probe. In this paper, we present a new method for calculating RHEED intensity spectra for rocking-curve analysis.

At energies as high as 10–40 keV, dynamical methods developed for low-energy electron diffraction (LEED) (Refs. 1–4) are no longer practical. In LEED calculations, the scattering by a single atom and among different atoms in a single layer or among different closely spaced layers[5] are solved using angular momentum basis functions [i.e., partial waves (l,m)]. There have been attempts to divide the layers into chains and treat the scattering in terms of cylindrical waves.[6,7] But the partial-wave method is no longer practical at RHEED energies because the number of basis functions needed increases rapidly as the energy increases (approximately as $E^{1/2}$). The method we use is based on expanding the scattering potential and wave function in the plane-wave representation. The basis vectors are the two-dimensional reciprocal-lattice vectors, $\mathbf{g}$, of the surface.

At high energies, electron scattering by an atom is confined primarily to a narrow cone whose central axis is the forward (unscattered) direction. Large-angle scattering outside the cone is small and therefore can be neglected. However, due to strong multiple scattering within the cone, kinematical theory cannot be used. For dynamical calculations, two sources of errors could occur in the plane-wave expansion. First, the number of Fourier coefficients $V_{\mathbf{g}}(z)$ of the scattering potential could be insufficiently included. The second source is insufficient inclusion of the basis functions, both propagating and evanescent ones.

Evanescent waves (or closed channels) are created at a scattering center and their amplitudes decay exponentially in the direction of propagation. At first glance, it is not obvious why *any* evanescent wave is needed in a calculation, since such a wave carries flux only a very short distance from where it is created. The importance of evanescent waves comes from the fact that there are many strong small-angle scatterings. Thus, over a short distance, an electron may scatter into an evanescent wave and scatter out again into a propagating wave, a number of times. This is how the effect of evanescent waves could be felt over a thickness of 10–15 Å, even though the wave itself may have long been attenuated. At an angle θ, the scattering cone is approximately 2θ, i.e., the scattering angle of the specular beam (see Fig. 1). Since evanescent waves lie at θ from the incident direction, a significant number of these must be included. Only evanescent beams that are very highly attenuated (i.e., large $\mathbf{g}$ components) can be neglected. These large $\mathbf{g}$ evanescent beams are so highly damped that their amplitudes have dissipated before any effective scattering can take place. Thus in an accurate calculation, both propagating and evanescent waves must be sufficiently included.

As we shall show later, the Schrödinger equation for RHEED takes the form of coupled second-order differential equations which are functions of z from the surface. In solving such equations, there are basically two categories of numerical approaches.[8] The first is called "solution following:" This consists of starting the

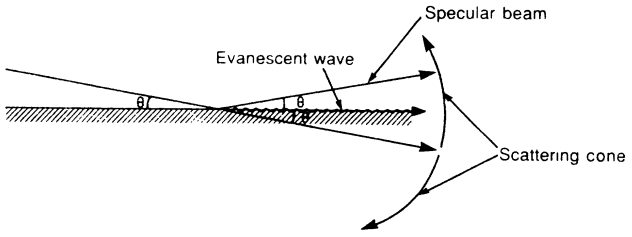

FIG. 1. Schematic diagram of the scattering angle between an evanescent beam and the incident beam.

equation solving at a region where the solution is easily obtainable. Then one proceeds to follow the solution numerically step by step into the asymptotic region where the boundary condition is applied. The method actually solves separately a wave function that propagates towards the surface and another that propagates away from the surface, at any given z. A prime example of this scheme is the Sams and Kouri method.[9] While the method is fast, it is plagued by numerical instabilities caused by evanescent (i.e., closed) channels. The problem comes from the fact that the solution is a linear combination of basis functions. If the basis functions contain closed channels which grow rapidly, the contributions of these channels may be orders of magnitude larger than the weakly growing ones. When this happens, round-off and truncation errors in the numerical process destroy the linear independence of the intermediate solutions. Thus, stabilization procedures must be applied at various steps to restore the linear independence of the solutions. However, when a number of closed channels with relatively large exponents are present, as often is the case in RHEED, the solution-following method may not work with any amount of stabilization. Or, even when it works, the stabilization step size becomes so small that the method is no longer practical. Previous RHEED calculations[10–15] used the solution-following scheme. Maksym[15] has recently introduced stabilization procedures based on the layer-doubling method of LEED.[2] However, this procedure is too cumbersome if stabilization has to be applied in a thickness less than one atomic layer (i.e., <2 Å). Thus, calculations based on the solution-following scheme are often "beam limited." As we shall see in Sec. VI, many results of previous calculations were nonconvergent.

The method we present here belongs to the invariant-embedding category[8] and is inherently more stable. The invariant-embedding method works by solving a quantity (in our case the ratio of the wave function and its first derivative, called the R matrix) by a recursion formula. Let us say that the R matrix for a combined $(i-1)$ slice has been solved. Then, the R matrix for the *combined* (i) slice is obtained by quantities related to the ith slice alone, together with the previous R-matrix solution of the combined $(i-1)$ slice. At each recursion step, the errors that destroy linear independence of the solutions are not allowed to propagate. Another important reason for the stability of the method is that the R matrix is the ratio of the wave function with its first derivative. Thus, the recursion steps do not explicitly involve wave functions. The R matrix is orders of magnitude better behaved numerically than the wave functions themselves.[16,17] This allows large steps to be taken (in regions where the potential is slowly varying) and explains why the method is computationally efficient. Finally, the R-matrix method does not decouple the wave function and its first derivative into an outward and an inward component. This separation is unnecessary inside the slab.

The invariant-embedding scheme is no longer beam limited. As we shall show in Sec. VI, our calculations are carefully tested for numerical convergence in terms of the number of beams needed. The R-matrix method with symmetric coupling matrices was introduced in atom-molecule collision theory.[8,16,17] In RHEED, the coupling matrices are generally Hermitian. In Sec. II, we shall describe the scattering potential used in our RHEED theory. The R-matrix method for RHEED is presented in Sec. III. The use of symmetry, the inclusion of temperature effects, and inelastic damping are described in Secs. IV and V, respectively. Convergent rocking-curve results for Ag(001) and Pt(111) are presented in Sec. VI. Section VII contains a summary.

In the R-matrix multislice method, the slices are made parallel to the surface. In a recent calculation by Peng and Cowley,[18] they sliced a slab normal to the surface. This normal-multislice method has many attractive features as it allows crystal imperfections parallel to the surface (i.e., a step) to be incorporated in a natural manner. The method, however, requires considerable computation time and, to date, there have been no rocking-curve calculations made.

II. THE SCATTERING POTENTIAL

We consider a surface slab made up of atomic layers, assuming two-dimensional periodicity such that

$$V(\mathbf{r})=V(\mathbf{r}+\mathbf{R}) \tag{1}$$

where $\mathbf{R}$ is a two-dimensional lattice vector. We expand the potential in Fourier series

$$V(\mathbf{r})=\sum_{\mathbf{g}} V_{\mathbf{g}}(z)e^{i\mathbf{g}\cdot\boldsymbol{\rho}} \tag{2}$$

where $\boldsymbol{\rho}$ and z are the Cartesian components of $\mathbf{r}$.

Consider a slab of N atomic layers. We select a slab unit cell which consists of a vertical column of atoms with thickness equal to that of the slab (see Fig. 2). The slab is made up of this column unit cell with two-dimensional translation vectors $\mathbf{P}$. Within this column unit cell, there are $s=1,2,\ldots,L$ atoms. We can now divide the slab into L planar (Bravais) lattices. Let $\mathbf{R}_0=(\mathbf{R}_\parallel,\mathbf{R}_z)$ be the coordinate of one of its atoms with respect to the master origin $\mathbf{O}$, and $\mathbf{R}_j$ be the lattice vector of the jth atom in the Bravais lattice. The vector $\mathbf{R}_j$ is in the set $\{\mathbf{P}\}$. Then we have

$$V(\mathbf{r})=\sum_j \phi(\boldsymbol{\rho}-\mathbf{R}_\parallel-\mathbf{R}_j,z-R_z) \tag{3}$$

where ϕ is the ion-core potential for the jth atom. From Eq. (2),

$$V_{\mathbf{g}}(z)=\frac{1}{A}\int_A V(\mathbf{r})e^{-i\mathbf{g}\cdot\boldsymbol{\rho}}d^2\rho \tag{4}$$

where A is the normalization area. Substituting (3) into (4) and changing the variable of integration from $\boldsymbol{\rho}$ to $\boldsymbol{\rho}'=\boldsymbol{\rho}-\mathbf{R}_\parallel-\mathbf{R}_j$, we obtain

$$V_{\mathbf{g}}(z)=\frac{1}{\Omega}\int_\Omega \phi(\boldsymbol{\rho}',z-R_z)e^{-i\mathbf{g}\cdot\boldsymbol{\rho}'}e^{-i\mathbf{g}\cdot\mathbf{R}_\parallel}d^2\rho' \tag{5}$$

where $\Omega=A/N$ is the two-dimensional unit-cell area and N is the number of unit cells in A. The potential function $\phi(\mathbf{r})$ can be expressed in terms of its Fourier transform

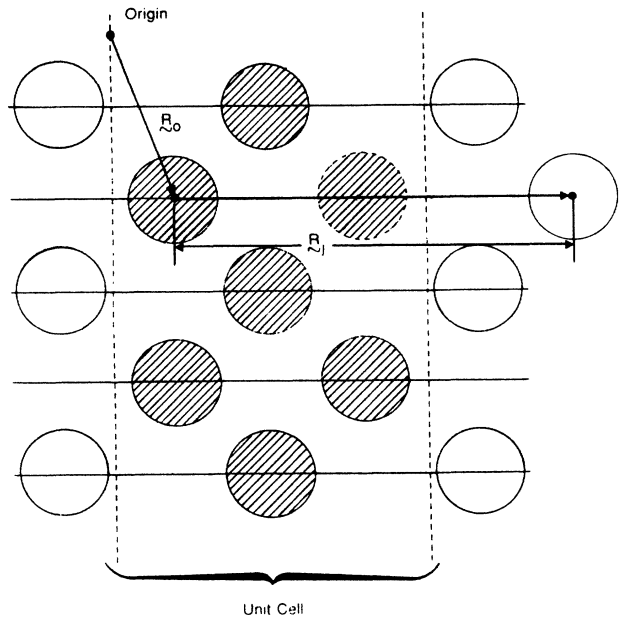

FIG. 2. Dividing a slab into column unit cells. The origins of the L Bravais lattices are at the centers of the hatched atoms.

$f_e(\mathbf{q})$ as

$$\phi(\mathbf{r})=\frac{\hbar^2}{4\pi^2 m}\int f_e(\mathbf{q})e^{i\mathbf{q}\cdot\mathbf{r}}d^3q \ . \tag{6}$$

Putting Eq. (6) into Eq. (5) and rewriting $\mathbf{q}=(\mathbf{q}_\parallel,\mathbf{q}_\perp)$, we obtain

$$\begin{aligned}V_{\mathbf{g}}(z)&=\frac{\hbar^2}{4\pi^2 m\Omega}e^{-i\mathbf{g}\cdot\mathbf{R}_\parallel}\\&\quad\times\int_\Omega d^2\rho\, e^{-i\mathbf{g}\cdot\rho}\int d^3q\, e^{i\mathbf{q}\cdot\mathbf{r}-iq_\perp R_z}f_e(\mathbf{q}_\parallel,q_\perp)\\&=\frac{\hbar^2}{m\Omega}e^{-i\mathbf{g}\cdot\mathbf{R}_\parallel}\int_{-\infty}^{\infty}dq_\perp\, e^{iq_\perp(z-R_z)}f_e(\mathbf{g},q_\perp) \ .\end{aligned} \tag{7}$$

We can fit the Fourier transform $f_e(q)$ by a sum of Gaussian functions, using a nonlinear fitting routine.[19,20] Thus if we write

$$f_e(q)=\sum_{i=1}^{n}a_i e^{-b_i q^2} \tag{8}$$

we obtain

$$V_{\mathbf{g}}(z)=\frac{\hbar^2}{m\Omega}e^{-\mathbf{g}\cdot\mathbf{R}_\parallel}\sum_{i=1}^{n}a_i\left[\frac{\pi}{b_i}\right]^{1/2}e^{-b_i g^2-(z-R_z)^2/4b_i} \ . \tag{9}$$

Since we treat the slab as composed of L Bravais lattices, we denote the origin of each lattice as

$$\mathbf{R}_s=(\mathbf{R}_{s\parallel},R_{sz}) \ . \tag{10}$$

Then for the slab we obtain

$$V_{\mathbf{g}}(z)=\frac{\hbar^2}{m\Omega}\sum_{i=1}^{n}\sum_{s=1}^{L}a_i(s)\left[\frac{\pi}{b_i(s)}\right]^{1/2}\times e^{-b_i(s)g^2}e^{-i\mathbf{g}\cdot\mathbf{R}_{s\parallel}-(z-R_{sz})^2/4b_i(s)} \tag{11}$$

where $[a_i(s),b_i(s),i=1,2,\ldots,n]$ are the Gaussian parameters for potentials in the sth Bravais lattice. For the calculation presented in this paper, $n=4$.

This procedure leaves one the freedom to choose the unit-cell scattering potential $\phi(\mathbf{r})$ as long as its Fourier transform can be fitted by a sum of Gaussians [i.e., via Eq. (8), but not necessarily confined to four Gaussians]. For $\phi(\mathbf{r})$, we have used Hartree-Fock atomic potentials.[19] We have also used self-consistent band-structure potentials based on the local-density-functional approach.[21] Results of these calculations are presented in Sec. IV.

III. THE INVARIANT-EMBEDDING METHOD FOR RHEED INTENSITIES

In order to calculate rocking-curve intensities, we need to find the reflection coefficients at the surface of the slab. By Bloch's theorem in two dimensions, one can write

$$\psi_{\mathbf{k}_\parallel}(\mathbf{r})=e^{i\mathbf{k}_\parallel\cdot\rho}U_{\mathbf{k}_\parallel}(\mathbf{r}) \tag{12a}$$

where $\mathbf{k}_\parallel$ is the parallel component of the wave vector of the incident electron. $U_{\mathbf{k}_\parallel}(\mathbf{r})$ is a function having the same periodicity as the potential and hence can be expanded as

$$U_{\mathbf{k}_\parallel}(\mathbf{r})=\sum_{\mathbf{g}}\phi_{\mathbf{g}}(z)e^{i\mathbf{g}\cdot\rho} \ . \tag{12b}$$

Substituting Eqs. (3) and (12) into Schrödinger's equation

$$\left[\frac{-\hbar^2}{2m}\nabla^2+V(\mathbf{r})\right]\psi(\mathbf{r})=E\psi(\mathbf{r}) \tag{13}$$

we obtain the following second-order coupled differential equation along the z direction for the Fourier expansion coefficients:

$$\phi_{\mathbf{g}}''(z)+\mathbf{k}_{\perp\mathbf{g}}^2\phi_{\mathbf{g}}(z)=\frac{2m}{\hbar^2}\sum_{\mathbf{g}'}V_{\mathbf{g}-\mathbf{g}'}(z)\phi_{\mathbf{g}'}(z) \tag{14}$$

where

$$\begin{aligned}\mathbf{k}_{\perp\mathbf{g}}^2&=\frac{2mE}{\hbar^2}-(\mathbf{k}_\parallel+\mathbf{g})^2\\&=\frac{2mE}{\hbar^2}-\mathbf{k}_{\parallel\mathbf{g}}^2 \ .\end{aligned} \tag{15}$$

Equation (14) is equivalent to the Schrödinger equation and can be written in matrix form as

$$\underline{\Phi}''(z)=\underline{W}(z)\underline{\Phi}(z) \tag{16}$$

where

$$\underline{\Phi}(z)=\begin{bmatrix}\phi_{g_1}(z)\\ \vdots\\ \phi_{g_i}(z)\\ \vdots\\ \phi_{g_N}(z)\end{bmatrix} \tag{17}$$

and

$$W_{gg'}(z)=\frac{2m}{\hbar^2}V_{g-g'}(z)-\mathbf{k}_{1g}^2\delta_{gg'} . \tag{18}$$

By taking the complex conjugate of Eq (2), it is easy to show that $V_{g-g'}$ is an Hermitian matrix, and hence $W_{gg'}$ is also Hermitian provided $\mathbf{k}_{1g}^2$ is real. For scattering problems, this is generally not the case because of inelastic damping. However, in Sec. V, we shall show how inelastic damping is included in the theory.

We now describe how the R-matrix solution to the coupled Eq. (16) may be constructed. We take the approach of dividing the crystal into thin slices (sectors) parallel to the surface. Inside each sector we determine a local R matrix, $\mathbf{r}$, and then a global R matrix is constructed by assembling the local R matrices. We start by dividing the slab into m slices, with the first slice at the bottom of the slab (see Fig. 3). The coupling matrix $\underline{W}$ is evaluated at the center of each slice and taken to be a constant over the entire width of the slice, i.e., if z_i is the center of the ith slice, we have,

$$W_{gg'}(z)=W_{gg'}(z_i)=W_{gg'}^{(i)} \tag{19}$$

for all z within the step. Since $\underline{W}^{(i)}$ is Hermitian, there exists a unitary transformation that diagonalizes the coupling matrix

$$\underline{T}^{(i)\dagger}\underline{W}^{(i)}\underline{T}^{(i)}=(\underline{\lambda}^{(i)})^2 \tag{20}$$

where $\underline{T}^{(i)\dagger}$ is the Hermitian conjugate of the transformation matrix $\underline{T}^{(i)}$. If we transform the plane-wave basis $\{\mathbf{\Phi}\}$ into a local basis $\{\mathbf{X}\}$ by

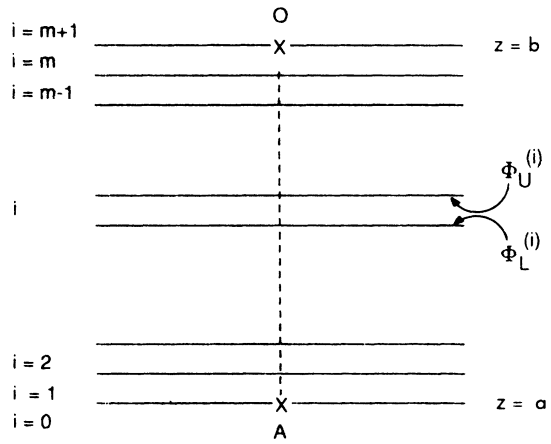

FIG. 3. Slicing a surface slab from O to A into m slices.

$$\underline{X}^{(i)}(z)=\underline{T}^{(i)\dagger}\underline{\Phi}^{(i)}(z) , \tag{21}$$

then in this local basis, Eq. (14) has the following form:

$$\underline{X}^{(i)''}(z)=(\underline{\lambda}^{(i)})^2\underline{X}^{(i)}(z) . \tag{22}$$

As $(\underline{\lambda}^{(i)})^2$ is a constant diagonal matrix within the ith sector, all the components of $\underline{X}^{(i)}$ are decoupled. For a single component, we have

$$X_g^{(i)''}(z)=(\lambda_g^{(i)})^2X_g^{(i)} , \tag{23}$$

which is a simple square-well problem. Its solution is given by the following relation (dropping the label g and sector label i):

$$X(z)=A\cosh(\lambda z)+B\sinh(\lambda z) \tag{24}$$

and its first derivative

$$X'(z)=A\lambda\sinh(\lambda z)+B\lambda\cosh(\lambda z) . \tag{25}$$

The choice of hyperbolic sine and cosine is unimportant and we could have easily chosen sine and cosine for the square-well problem. The consideration in choosing sinh and cosh is that λ would be complex if inelastic damping is taken into account.

Let L and U denote the bottom (lower) and top (upper) of the sector, respectively (see Fig. 3), then using Eqs. (24) and (25) it is easy to show

$$X_U=X_L\cosh(\lambda h)+\frac{X_L'}{\lambda}\sinh(\lambda h) \tag{26}$$

and its first derivative

$$X_U'=X_L\lambda\sinh(\lambda h)+X_L'\cosh(\lambda h) , \tag{27}$$

where $X_U=X(h)$ and $X_L=X(0)$ and h is the sector width. Rewriting Eqs. (26) and (27) in matrix form, we have

$$\begin{bmatrix}\underline{X}_L^{(i)}\\ \underline{X}_U^{(i)}\end{bmatrix}=\begin{bmatrix}\underline{r}_1^{(i)} & \underline{r}_2^{(i)}\\ \underline{r}_3^{(i)} & \underline{r}_4^{(i)}\end{bmatrix}\begin{bmatrix}-\underline{X}_L^{(i)'}\\ \underline{X}_U^{(i)'}\end{bmatrix} \tag{28}$$

where the local R-matrices $\underline{r}$ are defined as

$$\begin{aligned}(\underline{r}_1^{(i)})_{gg'}&=(\mathbf{r}_4^{(i)})_{gg'}=\lambda_g^{-1}\coth(\lambda_g h)\delta_{gg'} ,\\ (\underline{r}_2^{(i)})_{gg'}&=(\underline{r}_3^{(i)})_{gg'}=\lambda_g^{-1}\operatorname{csch}(\lambda_g h)\delta_{gg'} .\end{aligned} \tag{29}$$

To ensure the continuity of the total wave function and its normal derivative, we equate the wave functions and their derivatives of the ith and $(i-1)$th slices at the boundary,

$$\begin{aligned}\underline{X}_U^{(i-1)}&=\underline{Q}^{(i-1,i)}\underline{X}_L^{(i)} ,\\ \underline{X}_U'^{(i-1)}&=\underline{Q}^{(i-1,i)}\underline{X}_L'^{(i)} ,\end{aligned} \tag{30}$$

where $\underline{Q}^{(i-1,i)}=\underline{T}^{(i-1)\dagger}\underline{T}^{(i)}$. Note that the transformation matrix $\underline{T}$ is unitary and hence the matrix $\underline{Q}$ is also unitary. The transformation defined by Eq. (30) takes the local basis from sector $i-1$ to sector i (see Fig. 3).

The R-matrix scheme propagates by assembling the local R matrix defined in Eq. (29) recursively, beginning at the bottom of the slab and working towards the crystal-

vacuum interface. At each step of the recursion, a new global R matrix is obtained by assembling the new local R matrices from the old global R matrix. The global R matrix is defined as that which always relates the wave functions and derivatives at the outer boundary of the last sector assembled, so that

$$\underline{X}_U^{(i)}=\underline{R}^{(i)}\underline{X}_U'^{(i)} . \tag{31}$$

We note that in one component case, $\underline{R}^{(i)}$ is the inverse of the logarithmic derivative of $\underline{X}^{(i)}$. Therefore we expect $\underline{R}^{(i)}$ to be a smooth function of z. From Eqs. (29), (30), and (31), the recursion relation of the global R matrix is derived,

$$\underline{R}^{(i)}=\underline{r}_4^{(i)}-\underline{r}_3^{(i)}\underline{Z}^{(i)}\underline{r}_2^{(i)} , \tag{32a}$$

where

$$\underline{Z}^{(i)}=(\underline{r}_1^{(i)}+\underline{Q}^{(i-1,i)\dagger}\underline{R}^{(i-1)}\underline{Q}^{(i-1,i)})^{-1} . \tag{32b}$$

Recursively use of Eqs. (29), (30), (31), and (32) propagates the R matrix to the crystal-vacuum interface where the boundary condition is applied to obtain the RHEED intensity.

At the top side of the slab (outside), there are two waves: the incident wave

$$\psi_i(\mathbf{r})=\sum_{\mathbf{g}} C_{\mathbf{g}} e^{i\mathbf{k}_{\parallel\mathbf{g}}\cdot\rho} e^{-i\mathbf{k}_{\perp\mathbf{g}}z} , \tag{33a}$$

and the reflected wave

$$\psi_r(\mathbf{r})=\sum_{\mathbf{g},\mathbf{g}'} e^{i\mathbf{k}_{\parallel\mathbf{g}}\cdot\rho} e^{i\mathbf{k}_{\perp\mathbf{g}}z} M_{\mathbf{g}\mathbf{g}'}^{+-} C_{\mathbf{g}'} , \tag{33b}$$

where $\underline{C}$ is a column vector consisting of incident amplitude coefficients for the $\mathbf{g}$ beams and $\underline{M}^{+-}$ is the reflection matrix defined similarly as in LEED.[2-3] At the bottom of the slab, the transmitted wave could be written in terms of the transmission matrix $\underline{M}^{++}$ as

$$\psi_t(\mathbf{r})=\sum_{\mathbf{g},\mathbf{g}'} e^{i\mathbf{k}_{\parallel\mathbf{g}}\cdot\rho} e^{-i\mathbf{k}_{\perp\mathbf{g}}z} M_{\mathbf{g}\mathbf{g}'}^{++} C_{\mathbf{g}'} . \tag{33c}$$

Note that there is no reflection from below (below A, see Fig. 3). If we recall Eq. (12) and rewrite Eq. (33) in terms of the expansion coefficients [Eq. (12)], we have

$$\begin{aligned}\underline{\Phi}_i(z)&=\underline{I}(z)\underline{C} ,\\ \underline{\Phi}_r(z)&=\underline{Q}(z)\underline{M}^{+-}\underline{C} ,\\ \underline{\Phi}_t(z)&=\underline{I}(z)\underline{M}^{++}\underline{C} ,\end{aligned} \tag{34}$$

where $\underline{I}(z)$ and $\underline{Q}(z)$ are diagonal matrices with $e^{-i\mathbf{k}_{\perp\mathbf{g}_i}z}$ and $e^{i\mathbf{k}_{\perp\mathbf{g}_i}z}$ as the diagonal elements, respectively.

Propagation starts at the bottom of the slab, where the initial R matrix is obtained by taking the derivative of the transmitted wave and using the definition of the R matrix

$$(\underline{R}^{(0)})_{\mathbf{g}\mathbf{g}'}=i\mathbf{k}_{\perp\mathbf{g}}^{-1}\delta_{\mathbf{g}\mathbf{g}'} . \tag{35}$$

From the recursion relation of the R matrix [Eq. (32)], we obtain the R matrix at the inside surface of the slab, $\underline{R}^{(m)}$. In order to match the boundary condition at the surface, we change the basis functions from the local representation to the plane-wave representation, by the transformation defined in Eq. (21). Thus we obtain

$$\underline{\Phi}_b=\underline{R}^{(f)}\underline{\Phi}_b' \tag{36a}$$

where

$$\underline{R}^{(f)}=\underline{T}^{(m)}\underline{R}^{(m)}\underline{T}^{(m)\dagger} \tag{36b}$$

and $\underline{\Phi}_b$ is the wave function just below the interface.

Above the interface, the total wave function is the sum of the incident wave and the reflected wave. The boundary conditions require that the wave function and its first derivative be continuous, i.e.,

$$\begin{aligned}\underline{\Phi}_i(b)+\underline{\Phi}_r(b)&=\underline{\Phi}_b(b) ,\\ \underline{\Phi}_i'(b)+\underline{\Phi}_r'(b)&=\underline{\Phi}_b'(b) .\end{aligned} \tag{37}$$

Thus, from Eqs. (36) and (37) we obtain the reflection matrix

$$\underline{M}^{+-}=[\underline{R}^{(f)}\underline{Q}'(b)-\underline{Q}(b)]^{-1}[\underline{I}(b)-\underline{R}^{(f)}\underline{I}'(b)] . \tag{38}$$

The RHEED reflectivity for beam $\mathbf{g}$ is given by

$$R_{\mathbf{g}}^{\text{ref}}=\left|\frac{\mathbf{k}_{\perp\mathbf{g}}}{\mathbf{k}_{\perp 0}} M_{\mathbf{g}0}^{+-}\right|^2 . \tag{39}$$

The leading error in the numerical process depends on the derivative of the potential, which is assumed to be zero over the width of a sector. In order to reduce the error without sacrificing efficiency, it is necessary to control the sector width according to the variation of the potential.[16] One measure is to compute the rate of change of the average of the eigenvalues

$$V'=\frac{1}{N}\sum_{n=1}^{N}\frac{\lambda_n^2(i)-\lambda_n^2(i-1)}{z_i-z_{i-1}} . \tag{40a}$$

The new sector width is given by the following predictor:

$$h_{i+1}=\alpha V'^{-1/3} \tag{40b}$$

where α is a constant. At the minimum of the average of the eigenvalues, the above predictor overestimates the next sector's width. This problem is avoided by limiting the new sector width relative to the last sector, so that

$$h_{i+1}=\beta h_i . \tag{40c}$$

Another measure is to examine the $\underline{Q}$ matrix. For a truly constant potential, the $\underline{Q}$ matrix is unity. Therefore the quantity

$$C=\frac{\mathrm{Tr}(\underline{1}-\underline{Q})}{N(z_i-z_{i-1})^2} \tag{41a}$$

is a sensitive measure of the potential variation. The new sector width is given by

$$h_{i+1}=\gamma\left[\frac{N-1}{2C}\right]^{1/2} . \tag{41b}$$

The actual width is taken to be the minimum of the predictors discussed above. The final control over the actual

sector width used is to require a new sector to fall within a permissible range of sector width.

IV. SYMMETRY AMONG BEAMS

From the foregoing, it is clear that a major determining factor of the computation time is N, the number of beams included in the calculation. By use of symmetry, one can reduce the computation time by reducing the dimension of the matrices involved. In RHEED, the electron beam is incident on the surface at a glancing angle. This means that the only possible symmetry is the mirror plane symmetry when the incident beam coincides with a mirror plane.

From the unsymmetrized plane-wave basis $\{\phi\}$, we can construct a symmetrized basis[1] as follows

$$\chi_{\mathbf{g}}^{+}=\phi_{\mathbf{gg}} \quad \text{for } \mathbf{g}\in m \text{ (g on the mirror plane)},$$
$$\chi_{\mathbf{g}}^{\pm}=\frac{1}{\sqrt{2}}(\phi_{\mathbf{g}}\pm\phi_{\bar{\mathbf{g}}}) \quad \text{for } \mathbf{g}\in\bar{m} \text{ (g above the mirror plane)}, \tag{42a}$$

where $\bar{\mathbf{g}}$ is the mirror image of $\mathbf{g}$ and $\chi_{\mathbf{g}}^{+}$ with $\mathbf{g}\in m\cup\bar{m}$ is even and $\chi_{\mathbf{g}}^{-}$ with $\mathbf{g}\in\bar{m}$ is odd upon reflection by the mirror plane. As an example of how the use of symmetry reduces the computation, let us consider a two-beam case where the only beams are $\mathbf{g}$ and its mirror image $\bar{\mathbf{g}}$.

If we rewrite the transformation [Eq. (42a)] in matrix form,

$$\begin{bmatrix}\chi_{\mathbf{g}}^{+}\\ \chi_{\mathbf{g}}^{-}\end{bmatrix}=\underline{T}\begin{bmatrix}\phi_{\mathbf{g}}\\ \phi_{\bar{\mathbf{g}}}\end{bmatrix}, \tag{42b}$$

where

$$\underline{T}=\frac{1}{\sqrt{2}}\begin{bmatrix}1 & 1\\ 1 & -1\end{bmatrix} \tag{42c}$$

then the matrix $V_{\mathbf{gg}'}$ in Schrödinger's equation changes under the basis transformation [Eq. (42)] into

$$\underline{U}=\underline{T}\,\underline{V}\,\underline{T}^{-1}=\begin{bmatrix}V_{\mathbf{gg}}+V_{\mathbf{g}\bar{\mathbf{g}}} & 0\\ 0 & V_{\mathbf{gg}}-V_{\mathbf{g}\bar{\mathbf{g}}}\end{bmatrix}. \tag{43}$$

We note that the relation $V_{\mathbf{g}\bar{\mathbf{g}}}=V_{\bar{\mathbf{g}}\mathbf{g}}$ exists. Due to the block-diagonal form of Eq. (43), the antisymmetric basis function is independent of the symmetric basis function and can be dropped from the calculation, because it cannot be excited by an incident beam along a mirror plane. We note that this type of diagonalization is different from that discussed in the last section, where the diagonalization was done locally for each sector. Here the diagonalization is global to all sectors.

In general, under the transformation of basis defined by Eq. (42), the new potential matrix $\underline{U}$ is given by the following equation:[1]

$$U_{\mathbf{gg}'}=\left[\frac{J}{I}\right]^{1/2}\sum_{i=1}^{I}V_{\mathbf{gg}_i'} \tag{44a}$$

where I and J are the number of beams symmetrically related to $\mathbf{g}$ and $\mathbf{g}'$, respectively. Or, more explicitly, we can write

$$\begin{array}{c} \\ \mathbf{g}\in\bar{m}\\ \mathbf{g}\in m\end{array}\begin{array}{c}\begin{array}{cc}\mathbf{g}'\in\bar{m} & \mathbf{g}'\in m\end{array}\\ \begin{bmatrix}V_{\mathbf{gg}'}+V_{\mathbf{g}\bar{\mathbf{g}}'} & \sqrt{2}V_{\mathbf{gg}'}\\ \sqrt{2}V_{\mathbf{gg}'} & V_{\mathbf{gg}'}\end{bmatrix}\end{array}. \tag{44b}$$

The Schrödinger equation for the symmetrized basis functions takes the same form as in Eq. (14), except now the potential matrix $\underline{V}$ is substituted by the matrix $\underline{U}$. It is straightforward to show that the new potential matrix is also Hermitian. Therefore, the new equation can be solved in the same way as before, except that instead of solving N coupled equations, we now only need to solve $(N+N_m)/2$ equations. (N_m is the number of beams on the mirror plane). The initial R matrix in symmetrized basis is

$$(\underline{R}^{s})^{0}_{\mathbf{gg}'}=i\mathbf{k}_{\perp\mathbf{g}}^{-1}\delta_{\mathbf{gg}'}, \tag{45}$$

which is the same as Eq. (35). The relation between the reflection and R matrices in the symmetrized basis is

$$\underline{M}^{s+-}=[\underline{R}^{s(f)}\underline{Q}'(b)-\underline{Q}(b)]^{-1}[\underline{I}(b)-\underline{R}^{s(f)}\underline{I}'(b)], \tag{46}$$

which is the same as Eq. (38). A relation similar to Eq. (44) exists for the reflection matrix

$$M_{\mathbf{gg}'}^{s+-}=\left[\frac{J}{I}\right]^{1/2}\sum_{i=1}^{I}M_{\mathbf{gg}_i'}^{+-}. \tag{47}$$

Then the RHEED reflectivity for beam $\mathbf{g}$ is

$$R_{\mathbf{g}}^{\mathrm{ref}}=\left|\frac{\mathbf{k}_{\perp\mathbf{g}}}{\mathbf{k}_{\perp 0}}\;M_{\mathbf{g}0}^{+-}\right|^{2} \tag{48a}$$

and in terms of the symmetrized reflection matrix, it becomes

$$R_{\mathbf{g}}^{\mathrm{ref}}=\frac{1}{J}\left|\frac{\mathbf{k}_{\perp\mathbf{g}}}{\mathbf{k}_{\perp 0}}\;M_{\mathbf{g}0}^{s+-}\right|^{2} \tag{48b}$$

where for $\mathbf{g}\in\bar{m}$, $J=2$, or else $J=1$.

V. INELASTIC DAMPING AND TEMPERATURE CORRECTION

There are two factors which affect RHEED intensities that we have so far omitted: inelastic electron damping and temperature correction. In this section, we shall discuss their theoretical treatment. In LEED, inelastic damping is treated via the inclusion of a constant (position-independent) imaginary part in the scattering potential. The value of the constant imaginary potential is determined such that the calculated peak width matches the experimental width in an intensity-voltage (IV) spectra. In RHEED, inelastic damping may be treated by assuming a z-dependent imaginary potential, or a constant damping, or a full position-dependent imaginary potential.

For example, if we assume a z-dependent imaginary part, $i\epsilon V_I(z)$, then the total scattering potential $V'(\mathbf{r})$ is given by

$$V'(\mathbf{r})=V(\mathbf{r})+i\epsilon V_I(z) \tag{49}$$

where $V(\mathbf{r})$ is the real potential given in Eq. (2) and ϵ is a positive number to be chosen and $V_I(z)$ is the two-dimensional average of $V(\mathbf{r})$,

$$V_I(z)=\frac{1}{A}\int_A V(\boldsymbol{\rho},z)d^2\rho \ . \tag{50}$$

The Fourier expansion coefficients $V'_{\mathbf{g}}(z)$ are then given by

$$\begin{aligned} V'_{\mathbf{g}}(z)&=\frac{1}{A}\int_A [V(\boldsymbol{\rho},z)+i\epsilon V_I(z)]e^{-i\mathbf{g}\cdot\boldsymbol{\rho}}d^2\rho \\ &=V_{\mathbf{g}}(z)+i\epsilon\frac{4\pi^2}{A}V_I(z)\delta(\mathbf{g}) \\ &=V_{\mathbf{g}}(z)+i\epsilon V_I(z)\delta_{\mathbf{g}0} \ . \end{aligned} \tag{51}$$

The coupling matrix becomes

$$W'_{\mathbf{g}\mathbf{g}'}=W_{\mathbf{g}\mathbf{g}'}+i\epsilon\frac{2m}{\hbar^2}V_I(z)\delta_{\mathbf{g}\mathbf{g}'} \tag{52}$$

where $\underline{W}$ is the old coupling matrix given by Eq. (18). We note that the new coupling matrix is no longer Hermitian, since complex elements appear on the diagonal. However, because the complex part is independent of $\mathbf{g}$, we can separate it from the old coupling matrix to preserve its Hermitian property. In fact, if $\underline{T}$ diagonalizes the old coupling matrix $\underline{W}$,

$$\underline{T}^{\dagger}\underline{W}\,\underline{T}=\underline{\lambda}^2 \ , \tag{53}$$

it will also diagonalize the new coupling matrix $\underline{W}'$, since within each slice V_I is a constant

$$\underline{T}^{\dagger}\underline{W}'\underline{T}=\underline{\lambda}^2+i\epsilon\frac{2m}{\hbar^2}V_I\underline{I}=(\underline{\lambda}')^2 \ . \tag{54}$$

Therefore, unitary transformation exists for the matrix of the form given by Eq. (52). We note that a constant damping is just a special case of $\epsilon V_I(z)=V_I$.

If a crystal has a twofold rotation axis normal to the surface, then the Fourier expansion coefficients of the potential $V_{\mathbf{g}}$ are real. This is because a twofold rotation axis implies that $V_{\mathbf{g}}=V_{-\mathbf{g}}$. Remembering that the Fourier expansion of the form given by Eq. (2) has the general property $V^*_{\mathbf{g}}=V_{-\mathbf{g}}$, we obtain $V^*_{\mathbf{g}}=V_{\mathbf{g}}$.

Under the above condition, the total scattering potential may be chosen as

$$V'(\mathbf{r})=(1+i\epsilon)V(\mathbf{r}) \tag{55}$$

where ϵ is a positive number (usually taken as 0.1). Then the coupling matrix is complex symmetric. The matrix that diagonalizes the coupling matrix is orthogonal, having the property that $\underline{T}^{-1}=\underline{\tilde{T}}$. It is clear that an orthogonal transformation of the basis will decouple the Schrödinger equation (14). Therefore we need only to replace $\underline{T}^{\dagger}$ by $\underline{\tilde{T}}$ in the foregoing R-matrix formulation. Rocking curves using the different forms of inelastic damping are presented in the next section.

For crystals with general symmetry, we can use inelastic damping in the form given in Eq. (55) by requiring the eigenvector matrix to be nonsingular, i.e., that its inverse exists. For a physical problem, this is most likely to be the case. The consideration for Hermitian or symmetric coupling matrices is purely computational, since it would avoid explicit evaluation of inverses.

We include the temperature correction by multiplying each Fourier coefficient $V_{\mathbf{g}}$ by a Debye-Waller factor $D_{\mathbf{g}\mathbf{g}'}=e^{-M}$ where

$$M=\tfrac{1}{2}\langle(\Delta\mathbf{k}\cdot\Delta\mathbf{r})^2\rangle_T \ . \tag{56}$$

Here $\Delta\mathbf{k}$ is the momentum transfer of the scattering. The real part of $\Delta\mathbf{k}$ is taken, since it is the real part that gives rise to the wave interference on which the Debye-Waller factor is based. The momentum transfer $\Delta\mathbf{k}$ is defined as

$$\begin{aligned} \Delta\mathbf{k}_{\parallel}&=(\mathbf{g}-\mathbf{g}') \ , \\ \Delta\mathbf{k}_{\perp}&=\mathbf{k}_{\perp\mathbf{g}}\pm\mathbf{k}_{\perp\mathbf{g}'} \ , \end{aligned} \tag{57}$$

where $\mathbf{k}_{\perp\mathbf{g}}$ is given by Eq. (15).

Equation (57) shows an ambiguity: for an event that scatters an electron from $\mathbf{g}$ into $\mathbf{g}'$, there are two scattering paths associated with it, a small-angle path and a large-angle path. As mentioned in the Introduction, the amplitude for a large-angle scattering for a RHEED electron is extremely small. Thus, in the temperature correction, we only take the minus sign in Eq. (57). Anisotropy in the vibrational displacement amplitude of the surface atoms, i.e., the amplitudes perpendicular and parallel to the surface may be different, is included by expressing

$$M=\tfrac{1}{6}[\,|\,\Delta\mathbf{k}_{\parallel}\,|^2\langle(\Delta\mathbf{r}_{\parallel})^2\rangle_T+|\,\Delta\mathbf{k}_{\perp}\,|^2\langle(\Delta\mathbf{r}_{\perp})^2\rangle_T] \ . \tag{58}$$

The temperature-dependent coupling matrix $W^t_{\mathbf{g}\mathbf{g}'}$ is given by the following expression:

$$W^t_{\mathbf{g}\mathbf{g}'}=\frac{2m}{\hbar^2}D_{\mathbf{g}\mathbf{g}'}V_{\mathbf{g}-\mathbf{g}'}-\mathbf{k}^2_{\perp\mathbf{g}}\delta_{\mathbf{g}\mathbf{g}'} \ . \tag{59}$$

Insertion of this quantity in the appropriate equations yields temperature-corrected RHEED intensities.

VI. ROCKING CURVES FOR Ag(001) AND Pt(111) SURFACES

Rocking curves calculated by the R-matrix method for Ag(001) at $E=20\,000$ eV are shown in Figs. 4–8 for the (00), (01), (02), ($\bar{1}0$), and ($\bar{1}1$) beams, respectively. The incident electron is along the [110] azimuth. All interlayer spacings are set to the bulk value. The two-dimensional beam set used to obtain numerical convergence is shown in Fig. 9. The total number of beams used, adding together the solid and open circles, is 61. With mirror symmetry, the matrices are reduced to 36×36 square matrices according to equations given in Sec. IV. The Ag scattering potential is taken from the tabulation of Doyle and Turner.[19,20] The coefficients which control the thickness of each slice are given by $\alpha=\gamma=0.05$, $\beta=5$. This results in 60 to 80 slices per atomic layer. The choice of β limits that no new step size is to be more than or less than 5 times the previous step size. Numerical convergence is obtained at approximately seven atomic layers.

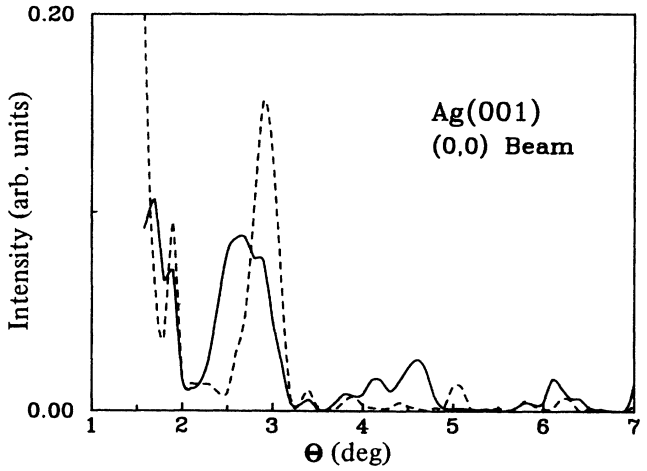

FIG. 4. The (00) beam rocking curve for Ag(001). Convergent result is represented by the solid curve, which uses the 61 beams indicated in Fig. 9. Dashed curve uses the 12 beams indicated in Fig. 9. The two curves are normalized in total area, resulting in the dashed curve $\times 3.0$.

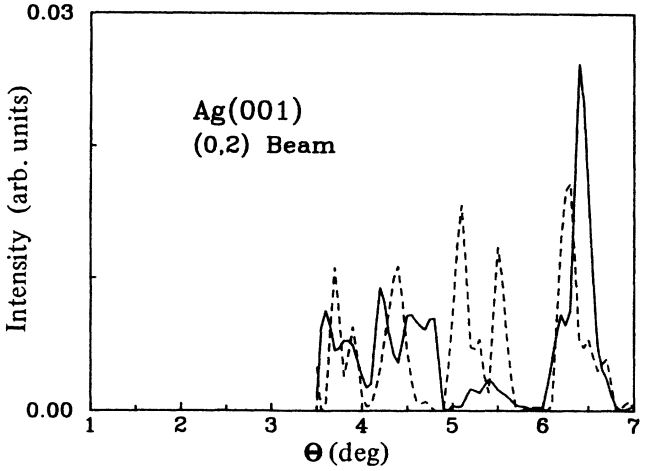

FIG. 6. Same as in Fig. 4, except for the (02) beam. The dashed curve $\times 7.8$.

The optical potential is taken to be $V_I(\mathbf{r})=0.1V_R(\mathbf{r})$, i.e., the factor $\epsilon=0.1$ in Eq. (55). In LEED, where muffin-tin potentials are used, the energy difference between the vacuum level and the potential of the flat regions outside the muffin-tin spheres is called the inner potential V_0. Note that V_0 is *not* the average potential inside a solid used in kinematical Bragg scattering analysis. At LEED energies, i.e., 50–400 eV, the value of V_0 varies between 7 and 14 eV. The major portion of this value comes from the exchange-correlation interaction (i.e., the real part of the electron self-energy) between the incident electron and the conduction electrons inside a solid.[3] The real part of the self-energy should *decrease* as the incident electron energy increases. The value of V_0 in RHEED is adjusted to optimize the comparison between calculated rocking curves with experiment, in much the same way as in LEED. In general, we expect the value of V_0 to be smaller in RHEED than in LEED. For rocking curves of Ag(001) using a superposition of Hartree-Fock atomic potentials, we used $V_0=0$ eV. Due to forward scattering and the small Debye-Waller factor, no temperature correction is included. In the figures, the solid curves represent convergent calculations, where the intensities would not change if more beams are added. As mentioned before, 61 beams symmetrized to 36 nonequivalent beams are used. The dashed curves are for calculations using the 12 beams indicated by open circles in Fig. 9. The same 12 beams were used in earlier publications.[10,11] It is clear that the 12-beam results are not convergent, as they show large differences in both peak intensity and position. Because the 12-beam calculated intensities are generally weaker, we have normalized the areas below the two curves in each figure. This allows the peaks in the 12-beam calculations to be clearly seen in the plots. The

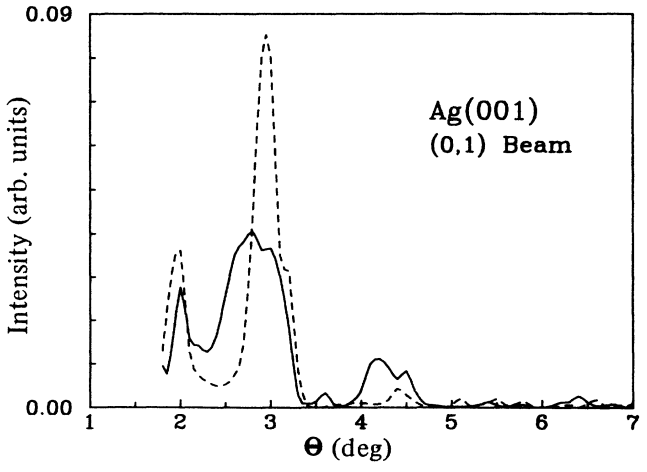

FIG. 5. Same as in Fig. 4, except for the (01) beam. The dashed curve $\times 2.1$.

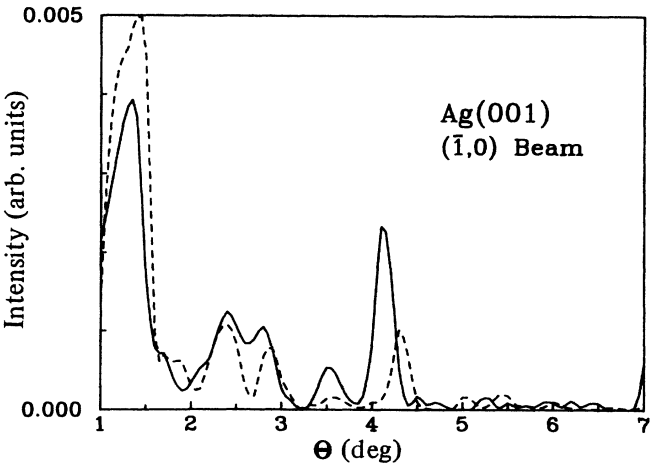

FIG. 7. Same as in Fig. 4, except for the $(\bar{1}0)$ beam. The dashed curve $\times 1.6$.

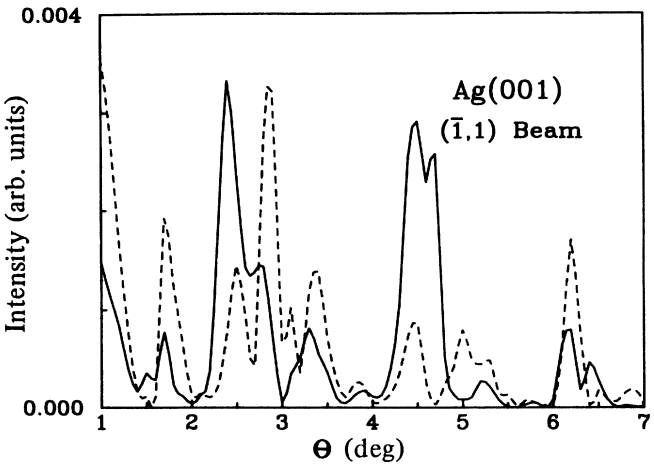

FIG. 8. Same as in Fig. 4, except for the $(\bar{1}1)$ beam. The dashed curve $\times 4.2$.

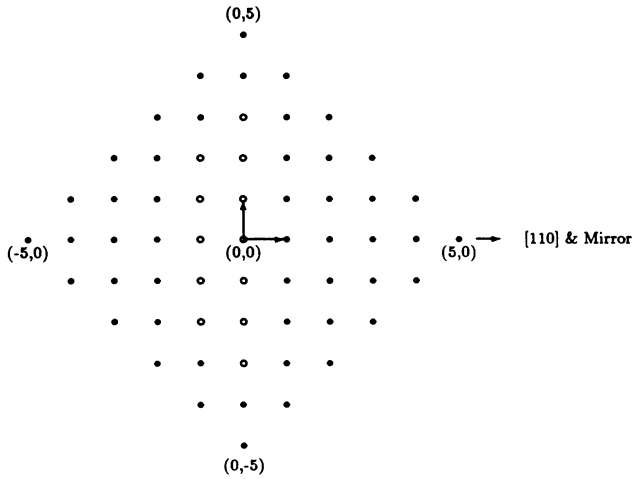

FIG. 9. Schematic diagram of incident azimuthal direction (arrow at far right). Convergent calculation requires 61 beams (open and solid circles). The 12-beam calculation uses beams represented by open circles only.

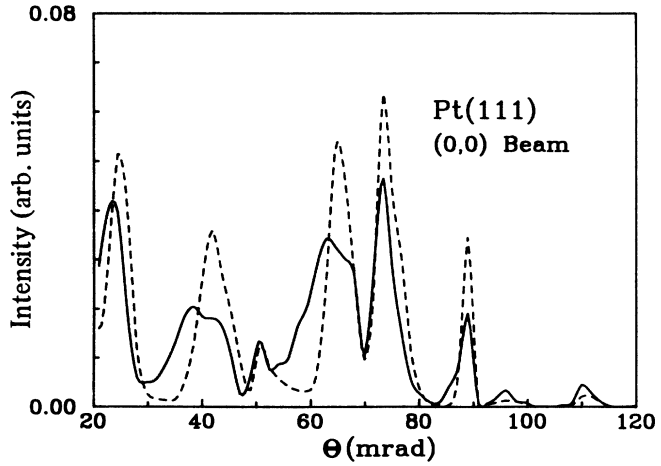

FIG. 10. The (00) beam rocking curve for Pt(111). Convergent result is represented by the solid curve. The dashed curve uses the 30 beams indicated in Fig. 11. The normalization factor is dashed curve $\times 1.9$.

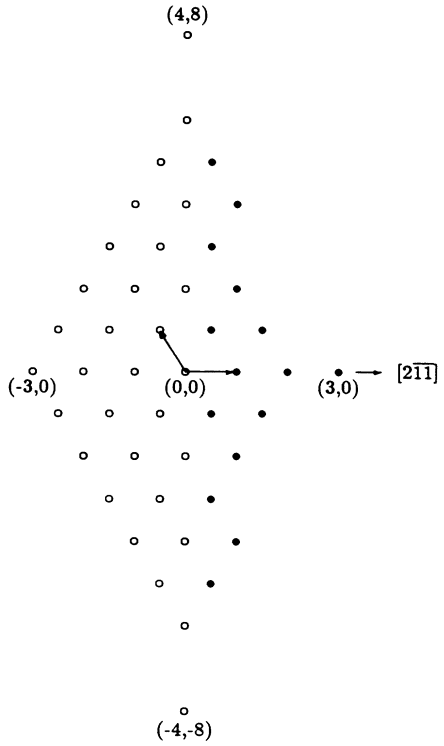

FIG. 11. Schematic diagram of the reciprocal space used for incident azimuthal direction along $[2\,\bar{1}\,\bar{1}]+32$ mrad azimuth. Convergent calculation uses the 45 beams represented by the open and solid circles. The 30-beam calculation uses beams represented by the open circles only.

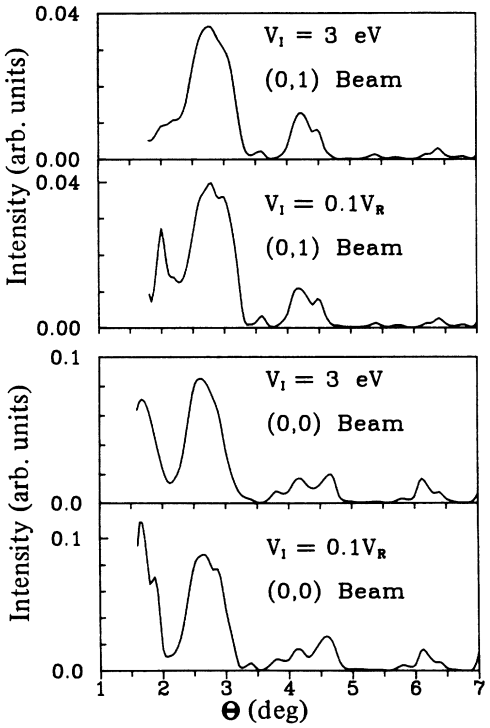

FIG. 12. Rocking curves for Ag(001) at $E=20\,000$ eV. for each beam, the upper panel uses a constant inelastic damping and the lower panel uses $V_I(\mathbf{r})=0.1V_R(\mathbf{r})$. The (00) and (01) beams are shown.

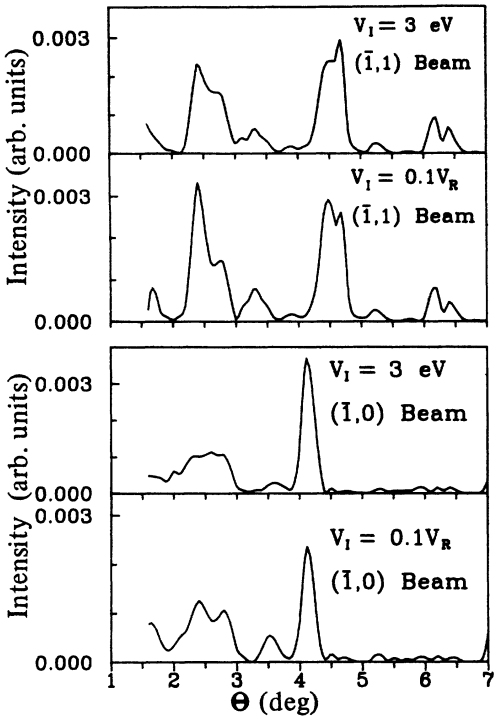

FIG. 13. Same as in Fig. 12, except for the $(\bar{1}0)$ beam and $(\bar{1}1)$ beams.

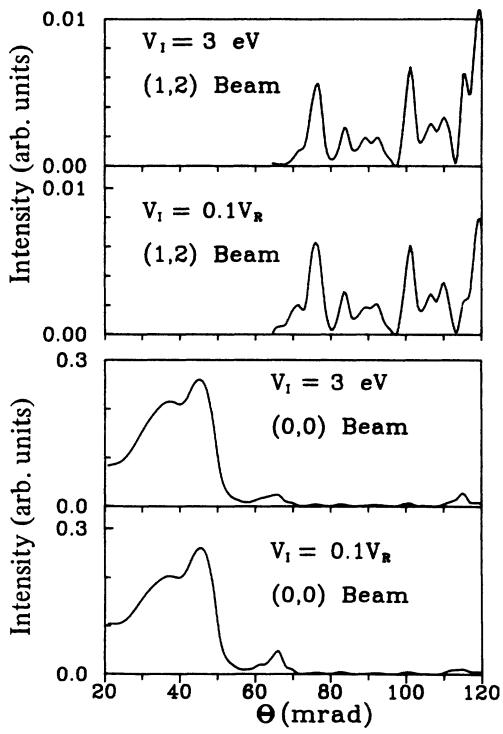

FIG. 14. Rocking curves for Pt(111) at $E = 19000$ eV. For each beam, the upper panel uses a constant inelastic damping and the lower panel uses $V_I(\mathbf{r}) = 0.1V_R(\mathbf{r})$. The (00) and (12) beams are shown.

normalization factor for each beam is given in the figure caption.

The rocking curve for Pt(111) at $E = 19000$ eV is shown in Fig. 10 for the (00) beam. The incident azimuthal direction is along $[2\,\bar{1}\,\bar{1}] + 32$ mrad. A slab of seven atomic layers is used. The surface interlayer spacing is contracted by 0.07 Å, while all deeper spacings are left at the bulk value. A self-consistent band-structure augmented-plane-wave (APW) Pt potential is used. The inner potential is $V_0 = 0$ eV and the imaginary potential is $V_I(\mathbf{r}) = 0.1V_R(\mathbf{r})$. The factors that control step size are set at $\alpha = \gamma = 0.05$ and $\beta = 5$. Again, no temperature correction is included. The solid curve is for the convergent calculation, using the 45 beams shown as open and solid circles in Fig. 11. The dashed curve is for including propagating and evanescent beams up to the zeroth Laue zone only (i.e., the 30 beams represented by open circles in Fig. 11). The results in Fig. 10 show the importance of including evanescent beams beyond the zeroth Laue zone for Pt(111). Otherwise, rather large errors in peak position and intensity would occur.

Since the optical potential $V_I(\mathbf{r}) = 0.1V_R(\mathbf{r})$ is an empirical model, we tested the dependence of rocking curves on its choice. In Figs. 12 and 13 we show rocking curves for Ag(001) with two choices of inelastic damping: $V_I = 3$ eV and $V_I(\mathbf{r}) = 0.1V_R(\mathbf{r})$. The calculations use 61 beams, so they are convergent. Other conditions are the same as those used in Figs. 4–8. We note that there are essentially no shifts in the peak positions. As expected, there are some differences in the absolute peak intensities. The largest difference occurs near the threshold angles [e.g., at $\theta \approx 2°$ for the (01) beam]. Half a degree or more above threshold, the two rocking curves are very similar. In Fig. 14, rocking curves for Pt(111) are shown, again for $V_I = 3$ eV and $V_I(\mathbf{r}) = 0.1V_R(\mathbf{r})$. For these calculations all interlayer spacings are set at the bulk value and 45 beams are used. Other conditions are the same as those in Fig. 10, except that the incident azimuthal direction is along $[2\,\bar{1}\,\bar{1}]$. Again, the rocking curves are very similar, especially the peak positions. From these analyses, we conclude that the imaginary part of the optical potential should be chosen with care, however, the details of the spatial variation in $V_I(\mathbf{r})$ should not be critical to the main features of RHEED rocking curves above 2°.

VII. SUMMARY

We have demonstrated the importance of reaching proper numerical convergence in calculating rocking curves and the capability of the R-matrix method in producing convergent calculations. With the R-matrix method, it is now possible to calculate accurately rocking curves for any strong scattering material. The calculated rocking curves are for *elastically* scattered electrons only, therefore, the experimental measurements should energy-filter out inelastic electrons for proper quantitative comparison with the theory. The relation of the peaks in rocking curves with interlayer diffraction and beam-emergent monolayer scattering and the use of the rocking curves for quantitative surface structure analysis are presented elsewhere.[22,23]

ACKNOWLEDGMENT

We would like to thank Dr. S. Nagano, Dr. Y. Huang, and Dr. K. A. Feng for programming help during the early stage of this work. Special thanks go to Dr. C. Schwartz for discussions concerning the *R*-matrix method. The computation was carried out at the National Center for Supercomputing Applications (NCSA) in Illinois. This work is supported by the National Science Foundation (NSF), under Grant No. DMR-84-05049, and by the donors of the Petroleum Research Fund (Grant No. 1154-AC5,6), administered by the American Chemical Society.

---

*Present address: The Blackett Laboratory, Imperial College of Science and Technology, University of London, London SW7 2BZ, Great Britain.

[1]M. A. Van Hove and S. Y. Tong, *Surface Crystallography by LEED* (Springer, Heidelberg, 1977).

[2]J. B. Pendry, *Low-Energy Electron Diffraction* (Academic, London, 1974).

[3]S. Y. Tong, Prog. Surf. Sci. **7**, 1 (1985).

[4]D. W. Jepsen, P. M. Marcus, and F. Jona, Phys. Rev. Lett. **26**, 1365 (1977).

[5]S. Y. Tong and M. A. Van Hove, Phys. Rev. B **16**, 1459 (1977).

[6]N. Masud and J. B. Pendry, J. Phys. C **9**, 1833 (1976).

[7]N. Masud, C. G. Kinniburgh, and D. J. Titterington, in *Determination of Surface Structure by LEED,* edited by P. M. Marcus and F. Jona (Plenum, New York, 1984).

[8]D. Secrest, in *Atom-Molecule Collision Theory,* edited by R. B. Bernstein (Plenum, New York, 1979).

[9]W. N. Sams and D. J. Kouri, J. Chem. Phys. **51**, 4815 (1969).

[10]P. A. Maksym and J. L. Beeby, Surf. Sci. **110**, 423 (1981).

[11]P. A. Maksym and J. L. Beeby, Surf. Sci. **149**, 157 (1985).

[12]P. A. Maksym and J. L. Beeby, Appl. Surf. Sci. **11/12**, 663 (1982).

[13]A. Ichimiya, Jpn. J. Appl. Phys. **22**, 176 (1983).

[14]H. Marten and G. Meyer-Ehmsen, Surf. Sci. **151**, 570 (1985).

[15]P. A. Maksym, in *RHEED and Reflection Electron Imaging of Surfaces,* edited by P. K. Larsen and P. J. Dobson (Plenum, New York, 1988).

[16]J. C. Light and R. B. Walker, J. Chem. Phys. **65**, 4272 (1976).

[17]E. B. Stechel, R. B. Walker, and J. C. Light, J. Chem. Phys. **69**, 3519 (1978).

[18]L. M. Peng and J. M. Cowley, Acta Crystallogr., Sect. A **42**, 545 (1986).

[19]P. A. Doyle and P. S. Turner, Acta Crystallogr., Sect. A **24**, 390 (1968).

[20]D. W. Marquardt, J. Ind. Appl. Math. **11**, 431 (1963).

[21]S. Y. Tong, T. C. Zhao, and H. C. Poon, in *RHEED and Reflection Electron Imaging of Surfaces,* edited by P. K. Larsen and P. J. Dobson (Plenum, New York, 1988).

[22]K. D. Jamison, D. N. Zhou, P. I. Cohen, T. C. Zhao, and S. Y. Tong, J. Vac. Sci. Technol. (to be published).

[23]T. C. Zhao and S. Y. Tong, Ultramicrosc. (to be published).